PAGEOPH, Vol. 133, No. 3 (1990)

0033-4553/90/030489-33$1.50 + 0.20/0

The Damage Mechanics of Brittle Solids in Compression

M. F. ASHBY[1] and C. G. SAMMIS[2]

Abstract—The development of microcrack damage in brittle solids in compression is analyzed, using a simple model. The model is developed from recent detailed analysis of the initiation, propagation and linkage of microfractures from pre-existing cracks, voids, or other inhomogeneities. It describes the evolution of damage with strain and from it a criteria for failure can be established. The results are used to construct failure surfaces in stress space which combine information about brittle failure with data describing the onset of plastic yielding. Such failure surfaces are constructed for a number of rocks and are compared with previously published experimental data.

Key words: Damage mechanics, brittle fracture, microcracks, fracture mechanics, rock mechanics, fracture nucleation, crack growth.

1. Introduction

When a brittle solid is loaded to failure, it does so by the propagation of cracks. The cracks nucleate and propagate from *inhomogeneities*, by which we mean holes, inclusions, microcracks, surface scratches or other defects. The difference between compressive and tensile fracture is that in tension a single crack grows unstably (once started, it accelerates across the sample to cause failure) while in compression a population of small cracks extends stably, each growing longer as the stress is raised, until they interact in some cooperative way to give final failure (Figure 1). Because of this, the strength of a brittle solid in compression is usually greater, by a factor of ten or more, than that in tension.

Measurements of the crushing strength of stone, brick and of cement must have been of interest to civil engineers since pre-Roman times. Systematic measurements of compressive strength really began about the middle of the last century (for its history, see JAEGER and COOK, 1976) but without much attempt to understand what determined it, or why brittle materials had useful strength in compression but none to speak of in tension. Elucidation of the mechanics of brittle tensile fracture

[1] Cambridge University Engineering Department, Trumpington Street, Cambridge CB2 1PZ, England.

[2] Department of Geological Sciences, University of Southern California, University Park, California 90089-0740, U.S.A.

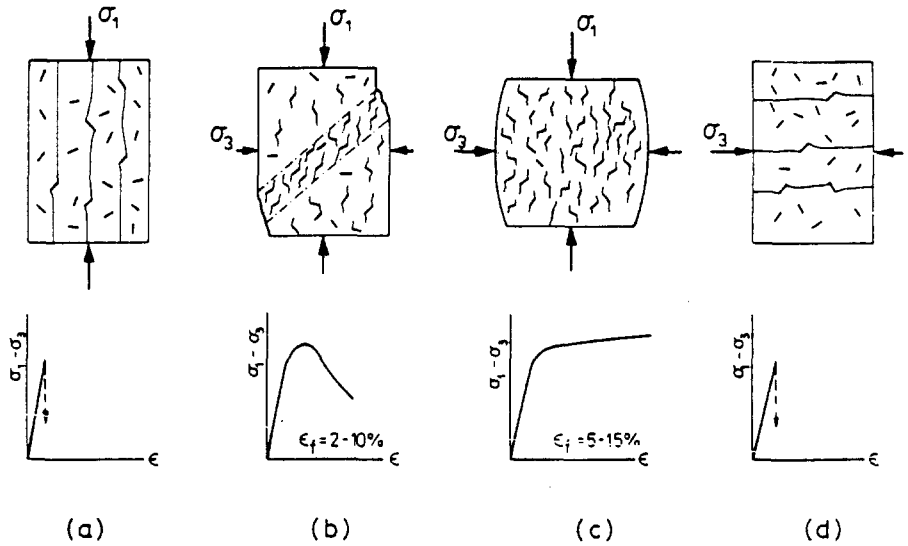

Figure 1
Compressive failure of a brittle solid containing a distribution of flaws.

has its roots in the work of GRIFFITH (1924), IRWIN (1958) and others that followed (see KNOTT, 1973, for a review), which has led to the development of *fracture mechanics* as a branch of engineering design.

The understanding of compressive brittle fracture is more recent, and still incomplete. A recent series of papers and reviews (GRIGGS and HANDIN, 1960; PATERSON, 1978; HALLBAUER *et al.*, 1973; TOPPONNIER and BRACE, 1976; WAWERSIK and FAIRHURST, 1970; WAWERSIK and BRACE, 1971; NEMAT-NASSER and HORII, 1982; NEWMAN, 1978; ASHBY and HALLAM, 1986; SAMMIS and ASHBY, 1986) have established that an isolated crack in a large body grows stably until its length becomes comparable with the dimension of the body itself; and that when many cracks are present (as they always are in natural rocks, in brick, in concrete and most ceramics) the cracks grow stably until their length is comparable with their spacing, when they interact, an instability develops, and the sample fails.

The problem can be complicated by time-dependent effects (ANDERSON and GREW, 1976; MARTIN, 1972; WAZA *et al.*, 1980; SANO *et al.*, 1981; COSTIN and HOLCOMB, 1981; ATKINSON and MEREDITH, 1987b), which have at least two origins. On the one hand crack growth can be limited by a chemical reaction, often with water. On the other, cracking in compression is associated with dilation; if the body is saturated with a fluid, then its flow into the dilating region can introduce a time-dependent aspect to fracture. In both cases, a static load which does not immediately cause failure may still do so if left in place for a sufficient length of time.

The understanding of compressive brittle fracture is still incomplete, but the mechanisms involved are much clearer than a decade ago. It seems an appropriate

time to try to abstract from the new observations and modelling a simplified description of compression-cracking, basing it as far as possible on the physical understanding. The goal is to develop a *damage mechanics of brittle solids*, from which the stress-strain response and an operational definition of failure can be derived for a material with a given set of elastic properties and given defect population, under a given state of stress. Two attempts to achieve this can be found in the open literature; that of COSTIN (1983, 1985), and that of SAMMIS and ASHBY (1986). Central to the problem is the relationship between stress and crack extension. COSTIN (1983, 1985) postulates a relationship of reasonable form, and develops from it expressions for the failure surface which (with some adjustable parameters) give a good description of the experimental data available at that time, but the model is not based on a physical model for crack growth. SAMMIS and ASHBY (1986) and ASHBY and HALLAM (1986) use methods of fracture mechanics to develop a physical model for crack extension, which they use to plot stress-strain curves for brittle solids from which failure surfaces can be constructed, but the complexity of their model makes the process cumbersome. In the present paper we attempt to develop a simpler, model-based mechanics of brittle compressive fracture, drawing heavily on the previous pieces of work.

2. Crack Initiation in Compression

Most brittle solids contain *inhomogeneities*: small holes or cracks, particles which are poorly bonded, or phases which have different moduli or strengths from those of the matrix. Any one of these can act as nuclei for new cracks when the solid is loaded.

The range of possible nuclei is wide, but the spectrum of their characteristics is probably bracketed by two extremes: the spherical hole and the sharp inclined crack (Figure 2). Both have been studied experimentally and both have been modeled, the first by SAMMIS and ASHBY (1986) and the second by NEMAT-NASSER and HORII (1982) and ASHBY and HALLAM (1986). In both cases, the criterion for crack initiation, under axisymmetric loading has the form

$$\sigma_1 = c_1 \sigma_3 - \sigma_0$$

where c_1 and σ_0 are material properties, σ_1 is the axial stress, and $\sigma_2 = \sigma_3$ the radial stress (both positive when tensile, negative when compressive).

In the later development of this paper we consider the growth of crack-damage from initial, inclined cracks as in Figure 2a. For this case (NEMAT-NASSER and HORII, 1982; ASHBY and HALLAM, 1986) cracks initiate when

$$\sigma_1 = \frac{(1+\mu^2)^{1/2}+\mu}{(1+\mu^2)^{1/2}-\mu}\sigma_3 - \frac{\sqrt{3}}{(1+\mu^2)^{1/2}-\mu}\frac{K_{Ic}}{\sqrt{\pi a}} \tag{1}$$

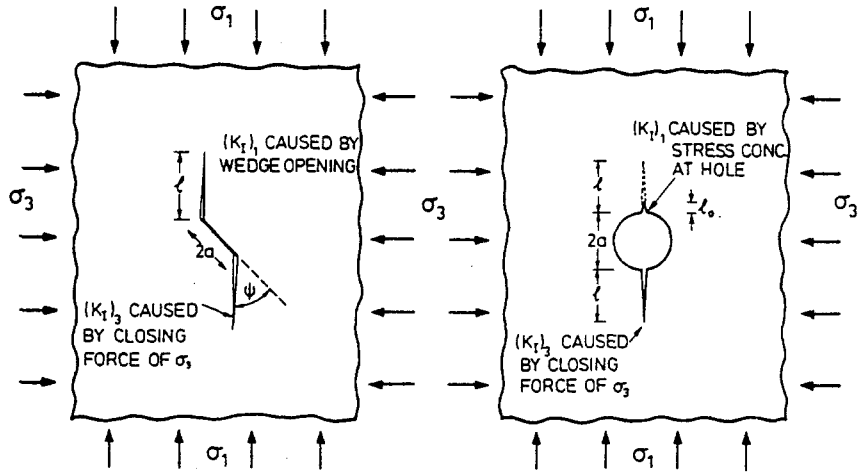

Figure 2
Cracks can initiate at inclined flaws and at holes. In both cases there are two contributions to K_I, the opening stress intensity at the tip of the growing wing cracks. One is caused by the stress concentrations at the flaw; the other is due to the closing effect of σ_3.

where μ is the coefficient of friction acting across the crack faces, K_{Ic} is the fracture toughness of the material through which the new crack propagates, and $2a$ is the length of the original inclined crack. Rocks, typically, show a coefficient of friction of about 0.6, in which case $C_1 = 3.1$ and $\sigma_0 = 3.1\, K_{Ic}/\sqrt{\pi a}$. Crack initiation from holes (SAMMIS and ASHBY, 1986) gives similar values.

Crack initiation can be detected in several ways: by the start of acoustic emission, by the first nonlinearity of the stress-strain curve, by the dilation of the sample, or by a sudden increase in internal friction. None give very accurate data, but they do allow a test of eq. (1). Figure 3 shows data for crack initiation in Westerly granite obtained by the first three techniques (HOLCOMB and COSTIN, 1986; BRACE *et al.*, 1966) plotted on axes of σ_1 and σ_3 to allow comparison with eq. (1). The linear relationship gives a good description of the data with a slope between 2.7 and 3.3 (corresponding to $\mu = 0.55$ to 0.64) and an intercept of 70–79 MPa (corresponding to a crack length $2a$ close to 1 mm when $K_{Ic} = 1$ MPa m$^{1/2}$).

The theory gives an adequate description of the data. It is used to describe the initiation of damage in the diagrams shown later. In each case, experimental data are fitted to eq. (1) to give μ and a (using published data for K_{Ic}). Results of this analysis are summarized in Table 1. In the computations, it is convenient to normalize the equations by the quantity $K_{Ic}/\sqrt{\pi a}$, giving

$$S_1 = c_1 S_3 - S_0 \tag{2}$$

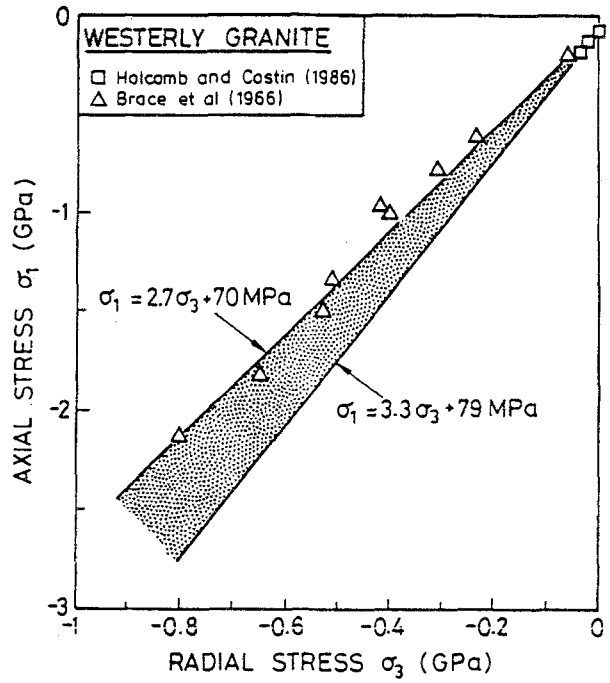

Figure 3
Data for crack initiation in Westerly granite. Crack initiation data for several other rocks are analyzed in Section 4. In all cases the data are well fitted by equation (1) with a coefficient of friction between 0.55 and 0.65.

with

$$S_1 = \sigma_1\sqrt{\pi a}/K_{Ic}$$
$$S_3 = \sigma_3\sqrt{\pi a}/K_{Ic}$$
$$c_1 = \frac{(1+\mu^2)^{1/2}+\mu}{(1+\mu^2)^{1/2}-\mu} \tag{3}$$
$$S_0 = \frac{\sqrt{3}}{(1+\mu^2)^{1/2}-\mu}.$$

3. Crack Growth and Interaction

Once initiated, the wing cracks (as we shall call the crack-like extensions of the original flaw) grow longer. During growth, the stress intensity K_I at the tip of each wing crack is equal to, or exceeds, the fracture toughness K_{Ic} of the solid. The condition for crack advance is simply

$$K_I \geq K_{Ic}.$$

Table 1

Material Properties of the Rocks and Fitted Model Parameters (Bracketted data are estimates)

Material(*)	K (GPa) (j)	E (GPa) (j)	Sy (MPa) (k)	K_{Ic} (MPa $m^{1/2}$) (l)	$2a$ (mm) (n)	μ (n)	D_0 (n)	C_3 (n)
ECLOGITE (a)	94	130	4000	(1.0)	0.6	0.6	0.08	2.0
DUNITE (b)	130	150	3500	(1.0)	1.0	0.6	0.04	2.0
APLITE (c)	58	—	2300	(1.0)	0.2	0.60	0.08	2.0
GABBRO (d)	60	92	2200	(1.0)	0.8	0.55	0.12	2.0
GRANITE (e)	58	70	2200	1.0	1.0	0.64	0.01	2.0
SANDSTONE (f)	130	130	1000	0.7	2.0	0.60	0.15	2.0
LIMESTONE (g)	70	77	700	0.6	0.05	0.55	0.15	2.0
MARBLE (h)	70	70	350	0.64	0.35	0.6	0.12	2.0
ROCKSALT (i)	37	37	65	0.23	0.5	0.55	0.20	2.0

(a) Eclogite; SHIMADA *et al.* (1983).
(b) Dunite; SHIMADA *et al.* (1983).
(c) Aplite; BRACE *et al.* (1966).
(d) Gabbro; SHIMADA *et al.* (1983).
(e) Westerly Granite; BRACE *et al.* (1966), MOGI (1966) and HOLCOMB and COSTIN (1986).
(f) Medium-grained Buntsandstone; GOWD and RUMMEL (1980).
(g) Solenhofen Limestone; HEARD (1960).
(h) Carrara Marble; VON KARMAN (1911) and EDMOND and PATERSON (1972).
(i) Rocksalt; HANDIN (1953) and HUNSCHE (1981).
(j) Bulk modulus K and Young's modulus E from BIRCH (1966).
(k) Derived from data plotted in Figures 11 to 24.
(l) ATKINSON and MEREDITH (1987). The lowest published value was chosen in each case.
(n) Obtained by fitting the data of Figs. 11 to 24 to the equations of the text.
(*) We assume $\alpha = 0.7$ and $\beta = 0.45$ for all materials.

The difference between tension and compression, as already mentioned, is that growth in compression is stable: each increment of crack advance requires an increment of load, at least until the cracks start to interact strongly. We will assume that a steadily increasing load drives the cracks at a steady rate, though in reality the inhomogeneity of natural materials may cause them to extend in little jumps. The problem, then, is to calculate K_I at the tip of the wing cracks.

3.1. Crack Growth from Starter Flaws of a Single Size: The 2-dimensional Case

Figure 4 shows an array of through-cracks, growing in a linear-elastic medium under a triaxial stress field σ_1, σ_3, positive when tensile, negative when compressive. Consider first the growth of a single isolated crack from an initial inclined flaw; interaction comes later. The upper inset of Figure 4 isolates one crack: it is made up of an initial crack of length $2a$ lying at an angle ψ to the X_1 direction with two wings, each of length l which (we will assume) lie parallel to X_1. The stress intensity at the tips of the wings is obtained approximately, but adequately, in the following way, based on the work of NEMAT-NASSER and HORII (1982), ASHBY and

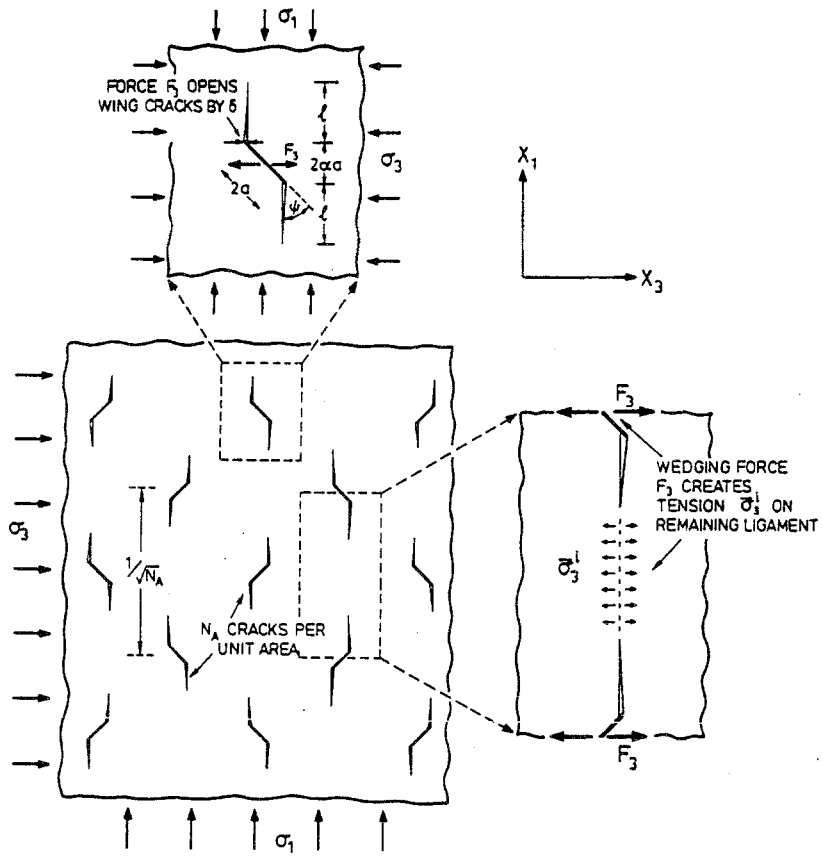

Figure 4
A population of growing cracks. We first analyze the growth of an isolated crack (shown above) and then include the crack-crack interaction (illustrated on the right).

HALLAM (1986), HORII and NEMAT-NASSER (1985, 1986), and KEMENY and COOK (1987).

The remote field σ_1, σ_3 creates a shear stress τ and a normal stress σ across faces of the initial crack. The crack slides (resisted by the coefficient of friction μ), wedging open the mouth of each wing crack by δ (Figure 4). The wedging can be thought of as caused by forces, F_3, parallel to X_3, acting at the midpoint of the crack. The stresses τ and σ are given by

$$\tau = \frac{\sigma_3 - \sigma_1}{2} \sin 2\psi \tag{4a}$$

$$\sigma = \frac{\sigma_3 + \sigma_1}{2} + \frac{\sigma_3 - \sigma_1}{2} \cos 2\psi. \tag{4b}$$

F_3 is simply the component of the sliding force acting parallel to X_3:

$$F_3 = (\tau + \mu\sigma)2a \sin\psi \tag{5a}$$

or

$$F_3 = -(A_1\sigma_1 - A_3\sigma_3)a \tag{5b}$$

where A_1 and A_3 are constants which depend on ψ, to be determined in a moment.

The force F_3, acting at the midpoint of a crack of length $2l$, creates a stress intensity tending to open the crack (TADA *et al.*, 1985, page 5.1) of

$$(K_I)_1 = \frac{F_3}{\sqrt{\pi l}}.$$

This result gives a good estimate of the stress intensity at the tip of a wing crack when l is large, but it breaks down (becoming infinite) when l is vanishingly small. The stress intensity at the tip of the initial inclined crack is not infinite, but can be calculated exactly as explained in the last section. We overcome this problem by introducing an "effective" crack length $(l + \beta a)$ giving

$$(K_I)_1 = \frac{F_3}{\sqrt{\pi(l + \beta a)}}. \tag{6}$$

We then choose β so that $(K_I)_1$ becomes equal to that for the inclined crack when l is zero.

Before doing this, we note that there is another contribution to K_I at the tip of the wing crack. The remote confining stress σ_3 acts not just on the angled crack but on the wing cracks of length l as well. In so doing, it produces an additional contribution to the stress intensity, tending to close the crack when σ_3 is compressive, of (TADA *et al.*, 1985, page 5.1):

$$(K_I)_3 = \sigma_3\sqrt{\pi l}. \tag{7}$$

Summing the two contributions, with F_3 given by eq. (5b), gives:

$$K_I = \frac{F_3}{\sqrt{\pi(l + \beta a)}} + \sigma_3\sqrt{\pi l} \tag{8a}$$

$$= -\frac{A_1\sigma_1\sqrt{\pi a}}{\pi\sqrt{L + \beta}} + \sigma_3\sqrt{\pi a}\left(\frac{A_3}{\pi\sqrt{L + \beta}} + \sqrt{L}\right) \tag{8b}$$

where $L = l/a$. The cracks extend until K_I becomes equal to K_{Ic}.

The constants are found by ensuring that this equation reduces to the exact result for crack initiation ($L = 0$) and matches the known results for very long cracks ($L \gg 1$), given by NEMAT-NASSER and HORII (1982) and ASHBY and

HALLAM (1986), eqs. (3) and (6). This gives

$$A_1 = \frac{\pi\sqrt{\beta}}{\sqrt{3}}((1+\mu^2)^{1/2} - \mu)$$

$$A_3 = A_1\left\{\frac{(1+\mu^2)^{1/2} + \mu}{(1+\mu^2)^{1/2} - \mu}\right\} \tag{9}$$

$$\beta = 0.1.$$

Equation (8b) with these values of A_1, A_3, and β (and with $K_I = K_{Ic}$) is plotted in Figure 5. It shows $\sigma_1\sqrt{\pi a}/K_{Ic}$ plotted against L with the earlier numerical results of NEMAT-NASSER and HORII (1982). Equations (8) are obviously a good approximation to the earlier calculations.

Now the interaction. The main part of Figure 4 shows an array of N_A cracks per unit area, all of which have extended to a length $2(l + \alpha a.)$ The center-to-center spacing of the cracks is

$$S = \frac{1}{\sqrt{N_A}} \tag{10}$$

so that an uncracked ligament of average length $S - 2(l + \alpha a)$ remains between the cracks in the X_1 direction. (Here α is simply a geometric constant, and must be distinguished from β; for cracks at 45° to X_1, $\alpha = 1/\sqrt{2}$). An opening force F_3 acts at the midpoint of each crack. Equilibrium requires that this opening force be balanced by a mean internal stress σ_3^i in the matrix, as shown in the right-hand side of Figure 4. The average internal stress is given by

$$\sigma_3^i = \frac{F_3}{S - 2(l + \alpha a)}. \tag{11}$$

This acts on the wing cracks, so that eq. (7) now becomes

$$(K_I)_3 = (\sigma_3 + \sigma_3^i)\sqrt{\pi l}. \tag{12}$$

We now define the initial damage D_0 and the current damage D by:

$$D_0 = \pi(\alpha a)^2 N_A \tag{13a}$$

$$D = \pi(l + \alpha a)^2 N_A \tag{13b}$$

giving

$$\sigma_3^i = \frac{-(A_1\sigma_1 - A_3\sigma_3)(D_0/\pi)^{1/2}}{\alpha(1 - 2(D/\pi)^{1/2})}. \tag{14}$$

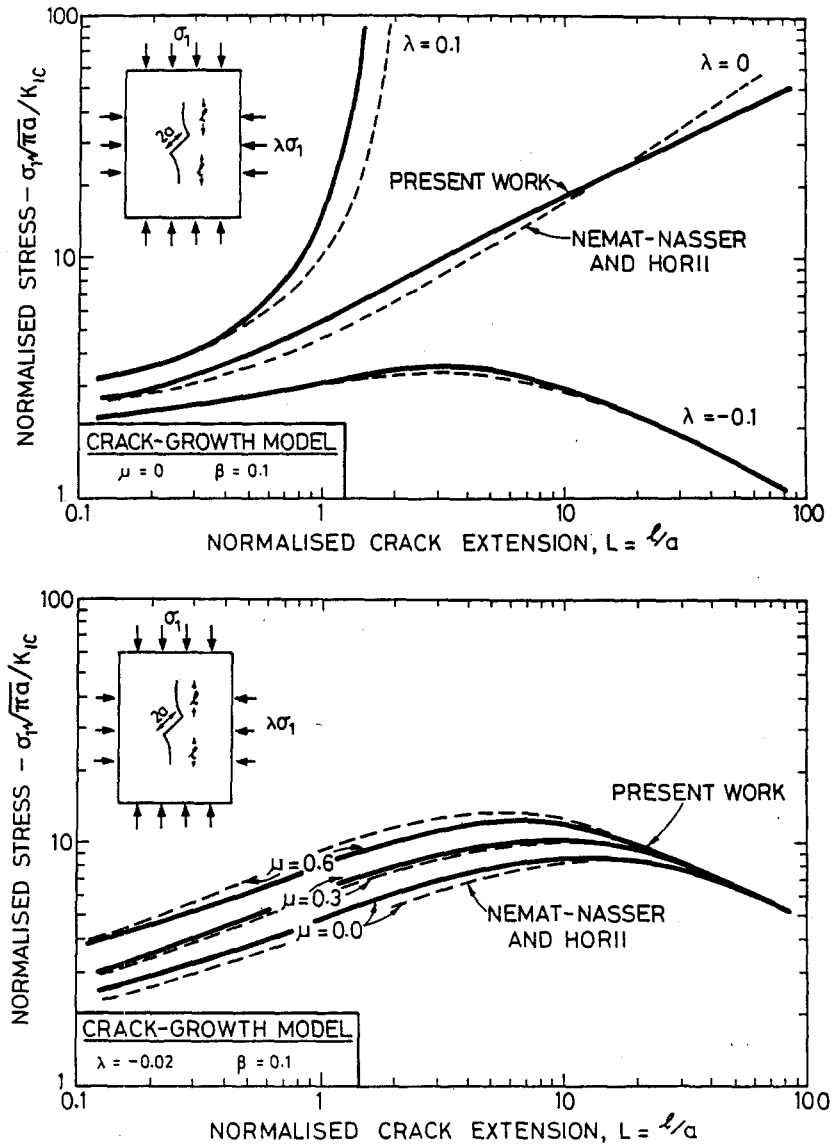

Figure 5
A comparison of the approximate equation (8b) with the numerical calculations of NEMAT-NASSER and HORII (1982). The approximation is adequate for the present purposes.

Equations (8a) and (8b) now become

$$K_I = \frac{F_3}{(\pi(l+\beta a))^{1/2}} + (\sigma_3 + \sigma_3^i)\sqrt{\pi l} \tag{15a}$$

$$= \frac{-A_1\sigma_1\sqrt{\pi a}}{\pi\sqrt{\alpha}\left(\left(\frac{D}{D_0}\right)^{1/2} - 1 + \frac{\beta}{\alpha}\right)^{1/2}} \left\{\left(1 - \frac{A_3}{A_1}\lambda\right)\left[1 + \left(\frac{\pi\left(\frac{D_0}{\pi}\right)^{1/2}}{1 - 2\left(\frac{D}{\pi}\right)^{1/2}}\right)\right.\right.$$

$$\left.\left. \cdot\left(\left(\frac{D}{D_0}\right)^{1/2} - 1\right)\right] - \frac{\pi\alpha\lambda}{A_1}\left(\left(\frac{D}{D_0}\right)^{1/2} - 1\right)\right\}. \tag{15b}$$

Here the first term in the curly brackets describes the wedging plus the crack-crack interaction; and the second term describes the closing effect of the lateral confining stress. The cracks propagate until K_I falls to K_{Ic}. Using this, rearranging and aggregating the constants (with $\sqrt{2/\pi} \approx 1$) gives for proportional loading (that is, with $\lambda = \sigma_3/\sigma_1$ held constant):

$$S_1 = \frac{-C_2\left(\left(\frac{D}{D_0}\right)^{1/2} - 1 + \frac{\beta}{\alpha}\right)^{1/2}}{(1 - C_1\lambda)\left\{1 + \frac{C_3 D_0^{1/2}}{(1 - D^{1/2})}\left(\left(\frac{D}{D_0}\right)^{1/2} - 1\right)\right\} - C_4\lambda\left(\left(\frac{D}{D_0}\right)^{1/2} - 1\right)} \tag{16}$$

and for loading at constant σ_3

$$S_1 = -\left[\frac{C_2\left(\left(\frac{D}{D_0}\right)^{1/2} - 1 + \frac{\beta}{\alpha}\right)^{1/2} - S_3\left[C_1\left(1 + \left(\frac{C_3 D_0^{1/2}}{1 - D^{1/2}}\right)\left(\left(\frac{D}{D_0}\right)^{1/2} - 1\right)\right) + C_4\left(\left(\frac{D}{D_0}\right)^{1/2} - 1\right)\right]}{1 + C_3\frac{D_0^{1/2}}{(1 - D^{1/2})}\left(\left(\frac{D}{D_0}\right)^{1/2} - 1\right)}\right] \tag{17}$$

where S_1 and S_3 are defined by equation (3). The values of the constants are

$$\begin{aligned} C_1 &= \frac{A_3}{A_1} = \frac{(1+\mu^2)^{1/2} + \mu}{(1+\mu^2)^{1/2} - \mu} \\ C_2 &= \frac{\pi\sqrt{\alpha}}{A_1} = \frac{\sqrt{3\alpha/\beta}}{(1+\mu^2)^{1/2} - \mu} \\ C_3 &= \sqrt{\pi} \\ C_4 &= \frac{\pi\alpha}{A_1} = \frac{\sqrt{3/\beta}}{(1+\mu^2)^{1/2} - \mu}. \end{aligned} \tag{18}$$

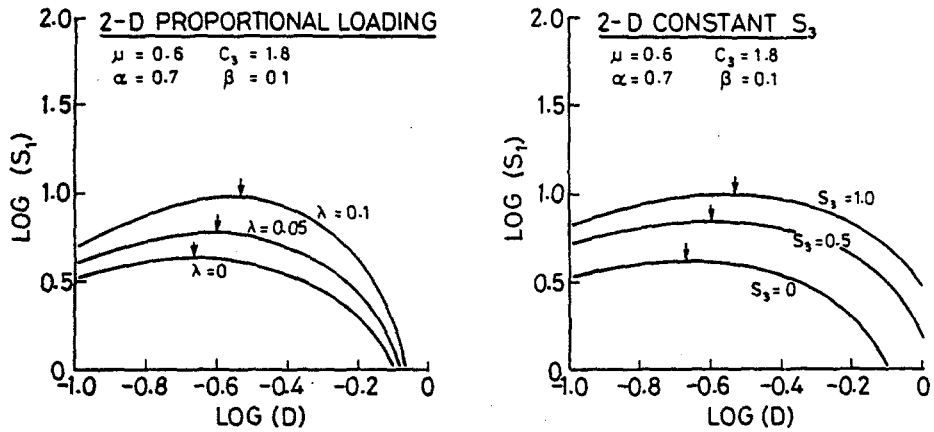

Figure 6
The dependence of axial stress on damage as predicted by equations (16) and (17). The peak stress is marked. We take this as the failure stress.

Figure 6 shows how the axial stress σ_1 varies with damage D for various confining pressures. The left-hand figure shows proportional loading; the right-hand figure, loading at constant σ_3. The peak stress, $(\sigma_1)_{max}$, rises and moves to the right as λ or σ_3 is increased. The shapes of the curves at constant λ differ from those at constant σ_3, as expected, but the *peaks* are at the same stress. Figure 7 shows $(\sigma_1)_{max}$ plotted against σ_3 for both conditions: the points lie on the same line.

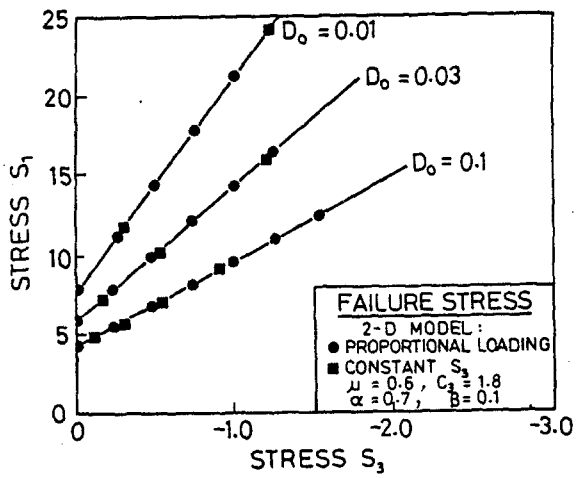

Figure 7
The peak value of σ_1 plotted against σ_3 to show the failure surface. In the present formulation, damage is a state variable.

3.2. Crack Growth from Starter Flaws of a Single Size: The 3-dimensional Case

It is usually the case that flaws are completely contained within the material. The merit of the 2-dimensional calculations developed in Section 3.2 is that it points to a way of tackling this more difficult 3-dimensional problem. We require the stress intensity at the periphery of a *contained* crack emanating from a starter flaw (which we take to be an inclined, penny-shaped crack) which we will equate, as before, to K_{Ic}. This we do by calculating the wedging force F_3 as in the 2-dimensional case. The wedging force creates an average internal stress σ_3^i. The stress intensity at the tip of a given wing crack is calculated from the wedging force and the total lateral stress $(\sigma_3 + \sigma_3^i)$, as shown in Figure 8. The significant difference to emerge in this 3-D calculation, when compared with earlier 2-D results is that the dependence of S_1 and S_3 on damage D involves different powers.

The wedging force F_3, as before, is calculated from the shear and normal stresses (eq. 4) acting on the initial plane, times the crack area, resolved into the X_3 direction:

$$\begin{aligned} F_3 &= (\tau + \mu\sigma)\pi a^2 \sin\psi \\ &= (A_1\sigma_1 - A_3\sigma_3)a^2. \end{aligned} \tag{19}$$

Unlike the 2-D case, there are no exact analytical solutions for limiting cases which allow A_1 and A_3 to be determined, so we make the assumption that they have the same values as before (eq. 9) but make provision to adjust them later to match experimental data.

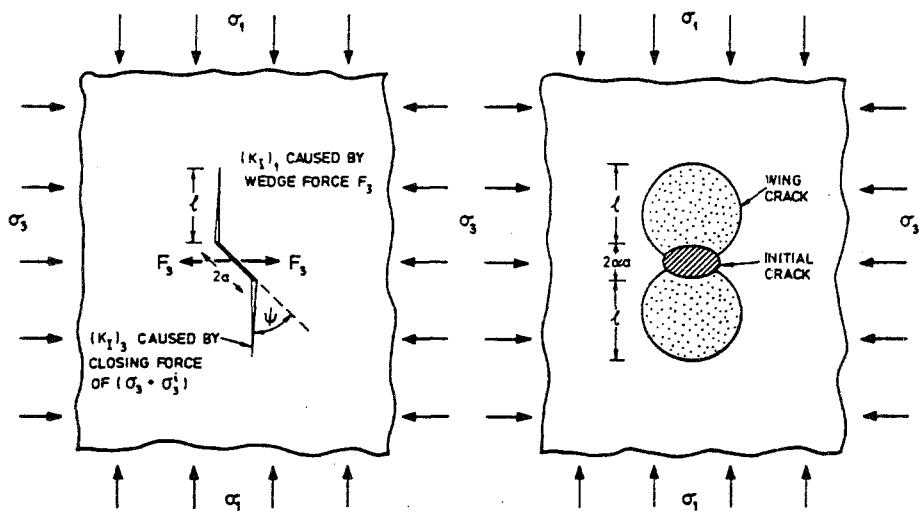

Figure 8

Wing cracks growing from an initial, constrained, penny-shaped flaw. The geometry is more complicated than in the 2-dimensional case but the same method can be used to give an approximate solution for K_I at the tips of the wing cracks.

The stress intensity K_I has the same three contributions as before. The wedging force F_3 induces a stress intensity which now has the form (TADA *et al.*, 1985, page 24.2)

$$(K_I)_1 = \frac{F_3}{(\pi(l+\beta a)^{3/2}} \tag{20}$$

where β is introduced for the same reason as before: to give a limiting value of $(K_I)_1$ when $l = 0$. The contribution due to σ_3 and σ_3^i are (TADA *et al.*, 1985, page 24.2).

$$(K_I)_3 = \frac{2}{\pi}(\sigma_3 + \sigma_3^i)\sqrt{\pi l}. \tag{21}$$

The internal stress for the 3-D case is

$$\sigma_3^i = \frac{F_3}{A - \pi(l+\alpha a)^2} \tag{22}$$

where $\pi(l+\alpha a)^2$ is the total crack area projected normal to X_3 and A is the area per crack

$$A = \pi^{1/3}\left(\frac{3}{4N_V}\right)^{2/3} \tag{23}$$

where N_V is the number of cracks per unit volume.

Damage is defined in a way which parallels that in two dimensions:

$$D_0 = \tfrac{4}{3}\pi(\alpha a)^3 N_V \tag{24a}$$

$$D = \tfrac{4}{3}\pi(l+\alpha a)^3 N_V \tag{24b}$$

giving

$$\sigma_3^i = \frac{-(A_1\sigma_1 - A_3\sigma_3)D_0^{2/3}}{\pi a^2(1-D^{2/3})}. \tag{25}$$

The stress intensity at the tip of the wing crack is

$$\begin{aligned} K_I &= \frac{F_3}{(\pi(l+\beta a))^{3/2}} + \frac{2}{\pi}(\sigma_3 + \sigma_3^i)\sqrt{\pi l} \\ &= \frac{-A_1\sigma_1\sqrt{\pi a}}{\pi^2\alpha^{3/2}((D/D_0)^{1/3} - 1 + \beta/\alpha)^{3/2}}\left\{\left(1 - \frac{A_3}{A_1}\lambda\right)\left[1 + 2(D/D_0)^{1/3} - 1)^2\left(\frac{D_0^{2/3}}{1-D^{2/3}}\right)\right]\right. \\ &\quad \left. - \frac{2\lambda}{A_1}\alpha^2\pi^2((D/D_0)^{1/3} - 1)^2\right\}. \end{aligned} \tag{26}$$

As before the crack propagate until K_I falls to K_{Ic}. Rearranging and aggregating the

constants give, for proportional loading:

$$S_1 = \frac{-C_2\left(\left(\frac{D}{D_0}\right)^{1/3} - 1 + \frac{\beta}{\alpha}\right)^{3/2}}{(1 - C_1\lambda)\left\{1 + \frac{C_3 D_0^{2/3}}{(1 - D^{2/3})}\left(\left(\frac{D}{D_0}\right)^{1/3} - 1\right)^2\right\} - C_4\lambda\left(\left(\frac{D}{D_0}\right)^{1/3} - 1\right)^2} \tag{27}$$

and for loading at constant σ_3

$$S_1 = -\left[\frac{C_2\left(\left(\frac{D}{D_0}\right)^{1/3} - 1 + \frac{\beta}{\alpha}\right)^{3/2} - S_3\left[C_1\left(1 + \left(\frac{C_3 D_0^{2/3}}{1 - D^{2/3}}\right)\left(\left(\frac{D}{D_0}\right)^{1/3} - 1\right)^2\right) + C_4\left(\left(\frac{D}{D_0}\right)^{1/3} - 1\right)^2\right]}{1 + C_3\frac{D_0^{2/3}}{(1 - D^{2/3})}\left(\left(\frac{D}{D_0}\right)^{1/3} - 1\right)^2}\right] \tag{28}$$

where S_1 and S_3 are defined by equations (3). The values of the constants are

$$\begin{aligned} C_1 &= \frac{A_3}{A_1} = \frac{(1+\mu^2)^{1/2} + \mu}{(1+\mu^2)^{1/2} - \mu} \\ C_2 &= \frac{\pi^2\alpha^{3/2}}{A_1} = \pi\alpha\sqrt{\frac{3\alpha}{\beta}}((1+\mu^2)^{1/2} - \mu)^{-1}. \\ C_3 &= 2 \\ C_4 &= \frac{2\alpha^2\pi^2}{A_1} = 2\alpha^2\sqrt{\frac{3}{\beta}}((1+\mu^2)^{1/2} - \mu)^{-1} \end{aligned} \tag{29}$$

The equations and constants have a form very like those of the 2-D model. Two significant differences should be noted. First, the extra dimension causes the powers of D which appear in the equation to differ (not surprisingly) from those of the 2-D model. Second, the constants C_1 to C_4 are not known with the same precision as those of the 2-D model because accurate limiting cases are not available to calibrate them. We shall assume (reasonably) that the dependence on the coefficient, μ, is properly included, but that the constant β may require further adjustment to give a good match with experiment.

Figures 9 and 10 illustrate some features of the results. The axial stress at first rises as damage grows (Figure 9), passing through a peak which shifts to higher values of damage as the confining pressure increases. The damage surface, shown in Figure 10, is almost a cone meaning that, to a first approximation, the failure envelope is described by

$$\sigma_1 = C\sigma_3 - \sigma_c$$

where C is a constant and σ_c is the unconfined compressive strength. The value of the model is that it gives a physical interpretation to C and σ_c, and relates them to the initial damage, the coefficient of friction, and the crack size.

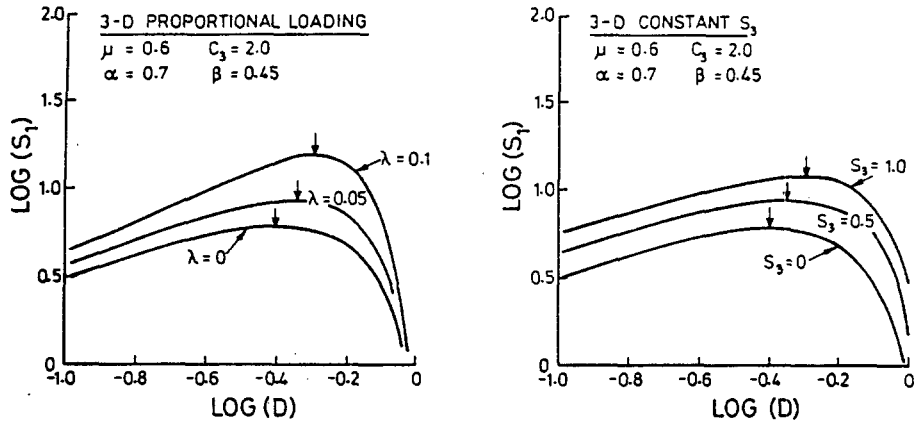

Figure 9
The dependence of axial stress on damage as predicted by equations (27) and (28). The peak stress is marked. We take this as the failure stress.

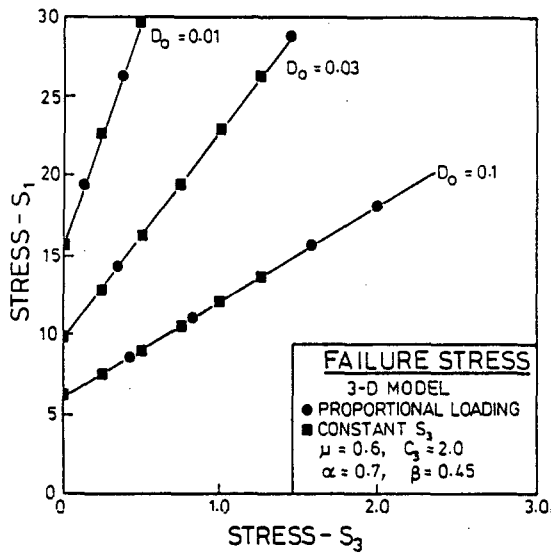

Figure 10
The peak value of σ_1 plotted against σ_3 to show the failure surface. In this formulation, damage is a state variable.

4. *Analysis of Data*

The strength of many different rocks has been determined under triaxial loading conditions ($|\sigma_1| > |\sigma_2| = |\sigma_3|$), where all three principal stresses are compressive). For a few, the initiation of microcracking has also been determined. We now apply

the damage mechanics model developed above to nine different rock types for which the most complete data sets exist: granite, aplite, dunite, eclogite, gabbro, sandstone, limestone, marble and rock salt. These rocks represent a wide range of composition and initial damage. Granite, aplite, dunite and eclogite are low porosity, crystalline, igneous rocks in which the initial damage is mostly in the form of low aspect cracks. Limestone and sandstone are porous sedimentary rocks in which the initial damage is mostly in the form of high aspect pores. Marble is a metamorphic rock with initial damage of a form intermediate between the previous two extremes. These rocks also span a wide range of yield strength. The igneous rocks have yield strengths in excess of 2 GPa while the calcareous rocks (limestone and marble) yield at stresses below 1 GPa. Rock salt is at the low extreme with a yield strength below 100 MPa.

The damage mechanics model formulated above has only one parameter β which is not physically related to the fractures. We have treated β as adjustable, choosing the vlaue 0.45 to give the best fit to the data. We assume $\alpha = 0.7$ (which corresponds to $\psi = 45°$).

For those materials where crack initiation data are available, the crack length $2a$ and the coefficient of friction μ are determined from the initiation surface (see Table 1)

$$\sigma_1 = C_1 \sigma_3 + \sigma_0$$

where C_1 and σ_0 are given by equation (1). The fracture toughness K_{Ic} and the initial flaw size $2a$ are also required. Although K_{Ic} may be estimated for most rocks (ATKINSON and MEREDITH, 1987a), the starter flaw size is not usually known and must be treated as an adjustable parameter. The derivation of the fundamental equations (27) and (28) from equation (26) gives $C_3 = 2$, and this gives a good description of the materials we have examined.

As the confining pressure is increased, brittle fracture is made increasingly difficult. A critical pressure may be reached at which true plasticity replaces crack extension. This transition can be illustrated by plotting a yield (or creep) surface, defined by:

$$\sigma_y^2 = \tfrac{1}{2}[(\sigma_1 - \sigma_2)^2 + (\sigma_2 - \sigma_3)^2 + (\sigma_3 - \sigma_1)^2]. \tag{30}$$

The yield surface is plotted as a pair of heavy broken lines on each figure. The yield strength, σ_y, can be derived from hardness, H, data since $\sigma_y = H/3$. The material properties and constants used to generate the theoretical initiation and failure curves are tabulated for each solid.

Consider, now, each material in turn. The triaxial data for damage initiation and failure are presented on plots of σ_1 vs σ_3. The theoretical fracture initiation surface (eq. 1), surfaces of constant damage, and the failure surface (calculated from the maximum of eq. (28) for each value of σ_3) and the yield surface are plotted on these graphs for comparison with the data.

4.1. Granite

Westerly granite is a fine-grained (0.75 mm), low porosity (0.9%), isotropic, two-mica calc-alkaline granite which has become a standard material in rock mechanics testing (see SCHOLZ, 1986, for a brief history). Mineralogical modal analyses are given by BIRCH (1960) and WAWERSIK and BRACE (1971).

Figure 11 shows theoretical surfaces for initiation, constant damage, and failure at low values of the confining stress. The fracture initiation data from BRACE *et al.* (1966) were determined from the onset of nonlinear behavior of the volume strain. Only data taken at the highest loading rate are plotted here in order to minimize effects of subcritical crack growth (which we do not model). The three initiation points from HOLCOMB and COSTIN (1986) were determined from the onset of acoustic emission (AE) in a previously unstressed sample. Also shown is a surface of constant damage mapped by HOLCOMB and COSTIN (1986) using the AE Kaiser effect as a probe. The triaxial failure data are from BRACE *et al.* (1966) and MOGI (1966).

Figure 12 shows the failure surface extended out to large values of the confining stress where it intersects the yield surface. Data at low and intermediate confining

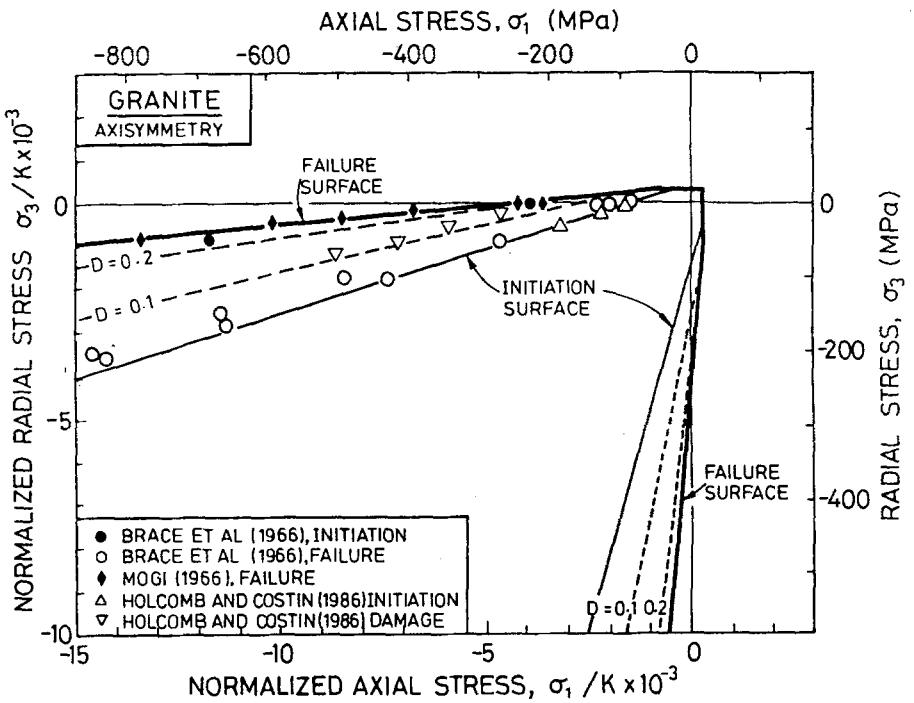

Figure 11
Comparison between experimental and theoretical failure surfaces for granite at low and intermediate confining stress. Data and theory for microfracture initiation and surfaces of constant damage are also compared. The yield surface (eq. 30) is also plotted as the heavy broken lines.

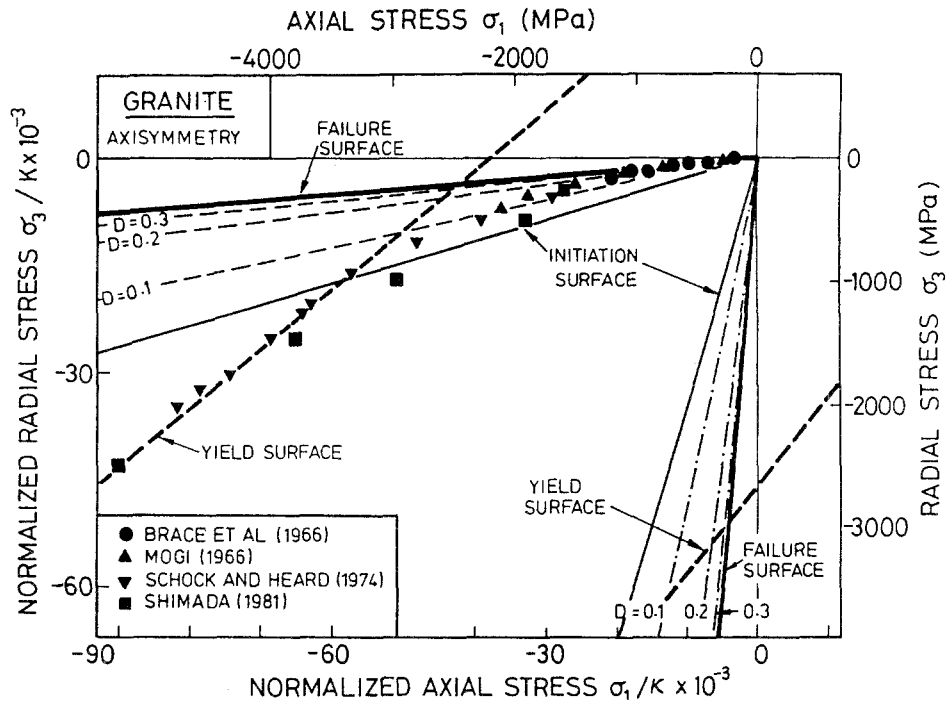

Figure 12
Comparison between experimental and theoretical failure surfaces for granite extended to the largest measured confining stress. Data and theory for microfracture initiation and surfaces of constant damage are also compared. The yield surface (eq. 30) is also plotted as the heavy broken lines.

pressures are from the same sources as in Figure 11. Those at high confining pressures are from SCHOCK and HEARD (1974) for Westerly granite and from SHIMADA (1981) for Man-nari granite (grain size 1–3 mm, apparent porosity: 0.7%). It is evident that the failure surface has considerable curvature and deviates from our theoretical model at high confining pressures. Although JANACH and GUEX (1980) have modeled this curvature in terms of the formation of shear bubbles at the grain boundaries, Figure 12 supports the possibility that the curvature is due to a gradual transition to ductile behavior. Analogous curvature is evident in subsequent figures for limestone, marble, and NaCl which are known to exhibit ductile behavior at moderate confining pressure, although the curvature in these rocks occurs over a more limited pressure range. The broader transition in granite may reflect its multimineralic composition for which the individual minerals have different brittle-ductile transition pressures. Note that the two granites show different transitional behavior at intermediate pressures, but that both approach the same ductile limit. Schock and Heard's observation that the stress-strain curve is linear to failure may be due to the convergence of the initiation and failure surfaces at very high confining pressures in Figure 12. The sudden release of energy and

shear localization at failure do not preclude stress concentration by ductile processes in the weaker minerals.

4.2. *Aplite*

BRACE *et al.* (1966) studied a quartz-oligoclase aplite (63% oligoclase, 27% quartz, and 10% biotite) which they described as fine-grained and flinty, apparently isotropic, and of high strength. The feldspar is highly altered. The grain size of the ground mass is about 40 μm and of the phenocrysts, about 100 μm. The small grain size and high strength are consistent with the small flaw size required by the model (see Figures 13 and 14). The relatively high initial damage is consistent with the flinty texture. A high density of small flaws may explain why flinty materials can be reliably fashioned into tools by flaking off small bits in a controllable manner.

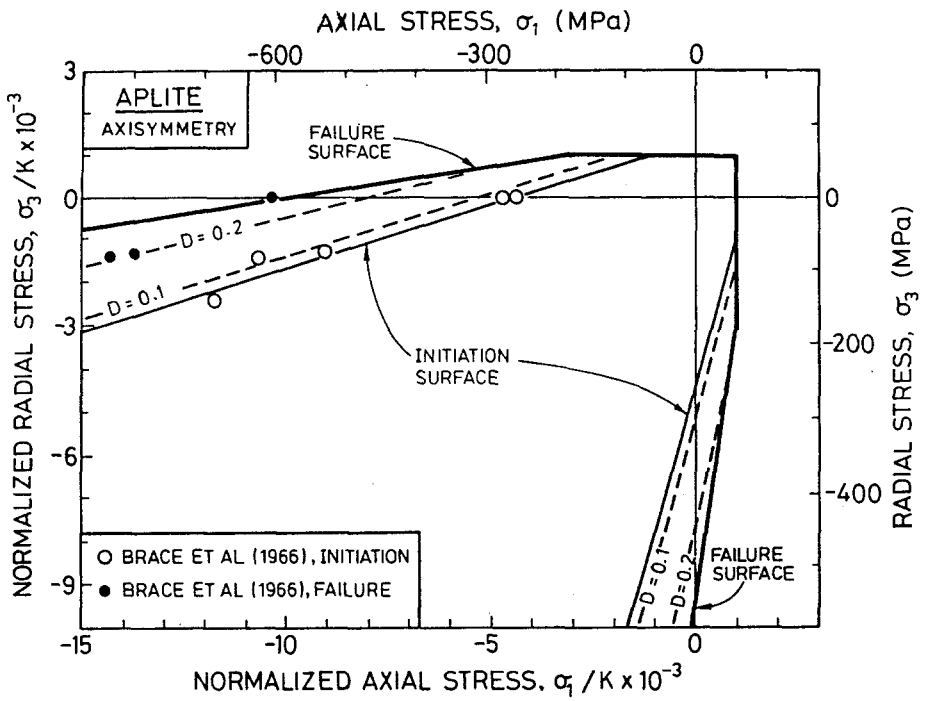

Figure 13

Comparison between experimental and theoretical failure surfaces for aplite at low and intermediate confining stress. The heavy solid line is the theoretical failure surface. The light solid line is the surface for the initiation of microfracturing while the light broken lines are surfaces of constant damage. The heavy broken line is the yield surface (eq. 30).

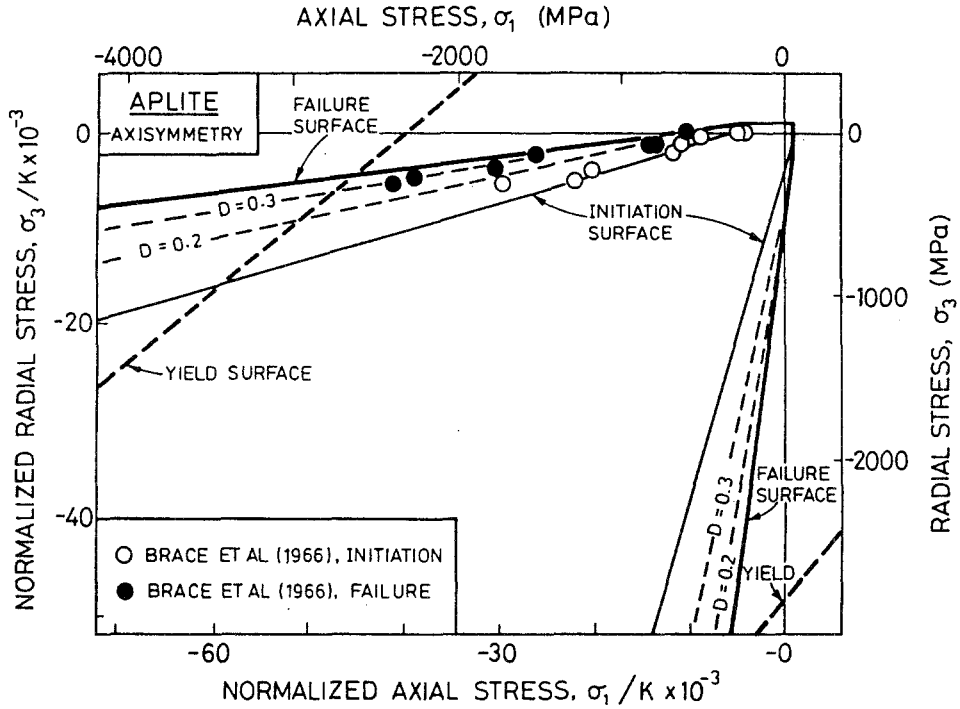

Figure 14

Comparison between experimental and theoretical failure surfaces for aplite extended to the largest measured confining stress. The heavy solid line is the theoretical failure surface. The light solid line is the surface for the initiation of microfracturing while the light broken lines are surfaces of constant damage. The heavy broken line is the yield surface (eq. 30).

4.3. Dunite

Dunite is an almost pure olivine rock. SHIMADA *et al.* (1983) measured the compressive strength of Horoman dunite (grain size 0.1–0.9 mm) at confining pressures up to 450 MPa, using a conventional triaxial testing apparatus, and to 3 GPa using a cubic press. Acoustic emissions showed a change in failure mode at confining pressures between 0.44 and 0.77 GPa. Below these pressures, acoustic activity increased rapidly between the onset of dilatancy and failure (the typical pattern for brittle failure). Above the transition pressure, and increase in acoustic activity was not observed to precede failure; rather, the level remained nearly constant up to failure. SHIMADA *et al.* (1983) correlate this change in behavior with the extreme curvature in the failure envelope. As is evident in Figure 15, our model suggests that this change in behavior is associated with the transition to plastic deformation.

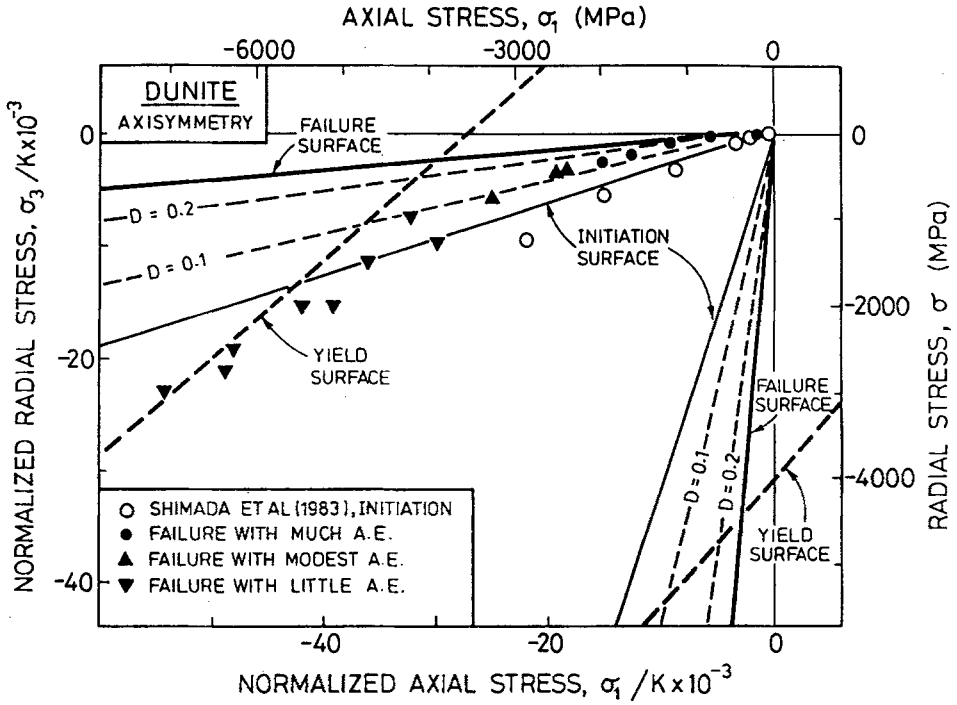

Figure 15

Comparison between experimental and theoretical failure surfaces for dunite. The heavy solid line is the theoretical failure surface. The light solid line is the surface for the initiation of microfracturing while the light broken lines are surfaces of constant damage. The heavy broken line is the yield surface (eq. 30).

4.4. Eclogite

Eclogite is an ultramafic pyroxene-garnet rock. The Akaishi eclogite measured by SHIMADA *et al.* (1983) was composed of 0.1–0.3 mm pyroxene grains and 0.8–2.3 mm garnet grains. It had a density of 3.642 Mg/m^3 and a porosity of 0.4%. Conventional triaxial tests covered a range of confining pressures from 0 to 450 MPa while tests in an opposed anvil cubic press extended the confining pressure to 3 GPa. As discussed above for dunite, the acoustic patterns indicate a change in failure mechanism at confining pressures between 1.02 and 1.99 GPa. The data and theoretical surfaces are given in Figure 16.

4.5. Gabbro

In addition to dunite and eclogite discussed above, SHIMADA *et al.* (1983) also studied Murotomisaki gabbro, a hypersthene-bearing-olivine-augite gabbro. The grain size of the olivine component is 1–2 mm, pyroxene is about 0.7 mm, and the plagioclase is about 0.7–3 mm. The bulk density is 2.985 Mg/m^3 and the reported

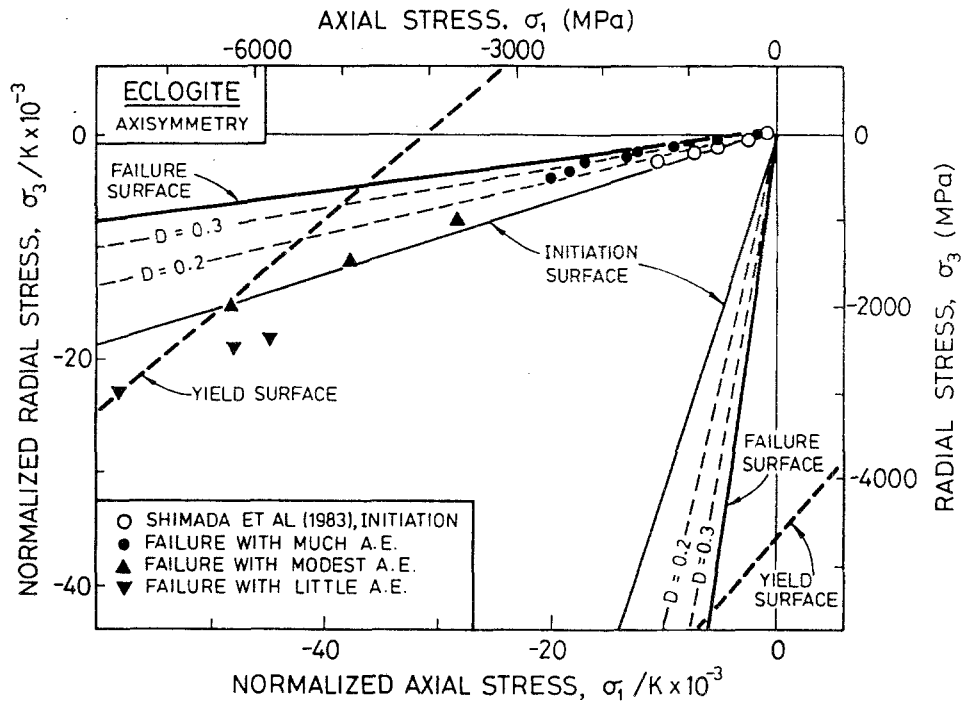

Figure 16

Comparison between experimental and theoretical failure surfaces for eclogite. The heavy solid line is the theoretical failure surface. The light solid line is the surface for the initiation of microfracturing while the light broken lines are surfaces of constant damage. The heavy broken line is the yield surface (eq. 30).

porosity is 0.4%. The acoustic pattern indicated a change in failure mechanism at confining pressures between 0.51 and 0.76 GPa. The data and theoretical surfaces are given in Figure 17.

4.6. Sandstone

The sandstone data in Figure 18 were obtained in triaxial compression by GOWD and RUMMEL (1980). The rock is described as a medium grain-sized Buntsandstone from SW-Germany with subangular to round quartz grains bedded within a clayey matrix. Its initial porosity was 15% with an initial permeability of 50 microdarcy. The damage initiation data were defined by the onset of dilatancy. At confining pressures above about 30 MPa, the stress-strain curves are nonlinear at lower values of the axial stress than the observed onset of dilatancy. This probably reflects the suppression of dilatancy by pore collapse, a phenomenon which the authors propose to explain the total lack of observed dilatancy at the highest confining pressures. Such effects are beyond the scope of our model.

A transition from brittle failure to apparent ductile shear deformation takes

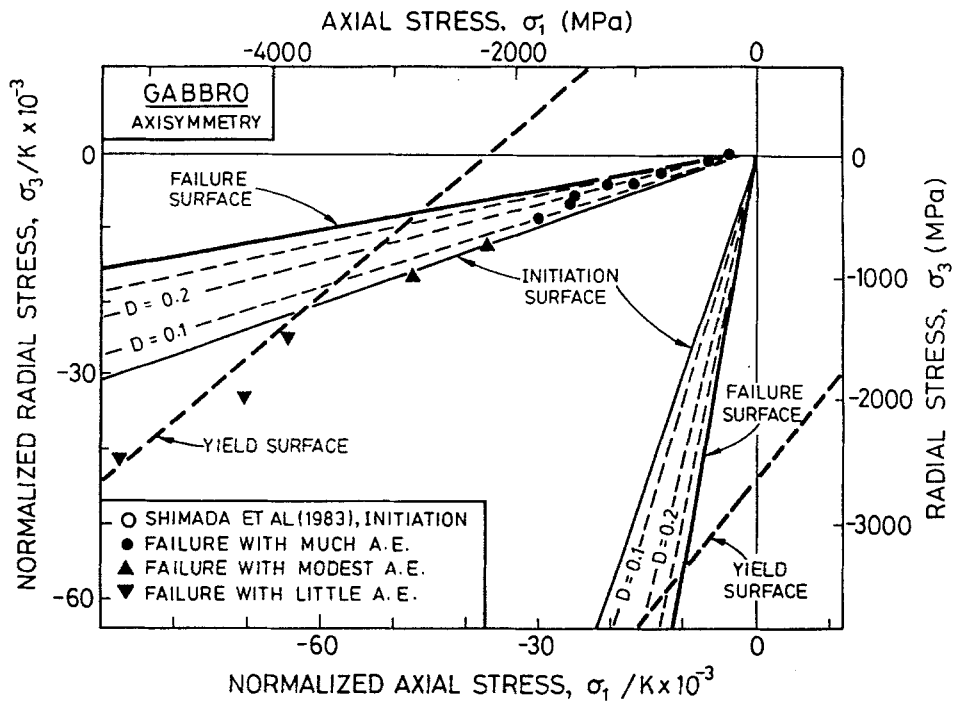

Figure 17
Comparison between experimental and theoretical failure surfaces for gabbro. The heavy solid line is the theoretical failure surface. The light solid line is the surface for the initiation of microfracturing while the light broken lines are surfaces of constant damage. The heavy broken line is the yield surface (eq. 30).

place at a pressure of about 100 MPa. However, the observed pressure dependence of the flow stress for confining pressures in excess of 100 MPa argues against true ductile flow and for a cataclastic mode of deformation probably involving pore collapse. Dilatancy at failure is a constant for confining pressures between 0 and 40 MPa. From 40 to 100 MPa, dilatancy at failure decreases to zero. Above 100 MPa, brittle failure does not occur.

4.7. Limestone

Solenhofen limestone is a fine grained (0.01 mm) mechanically isotropic limestone from Bavaria. It has a connected porosity of 5.3% and a total porosity in the range 6–9% (RUTTER, 1972). The strength data in Figure 19 are from HEARD (1960) and include both triaxial compression and tension. The fracture initiation points were picked as the onset of nonlinearity in his published stress-strain curves and are only approximate.

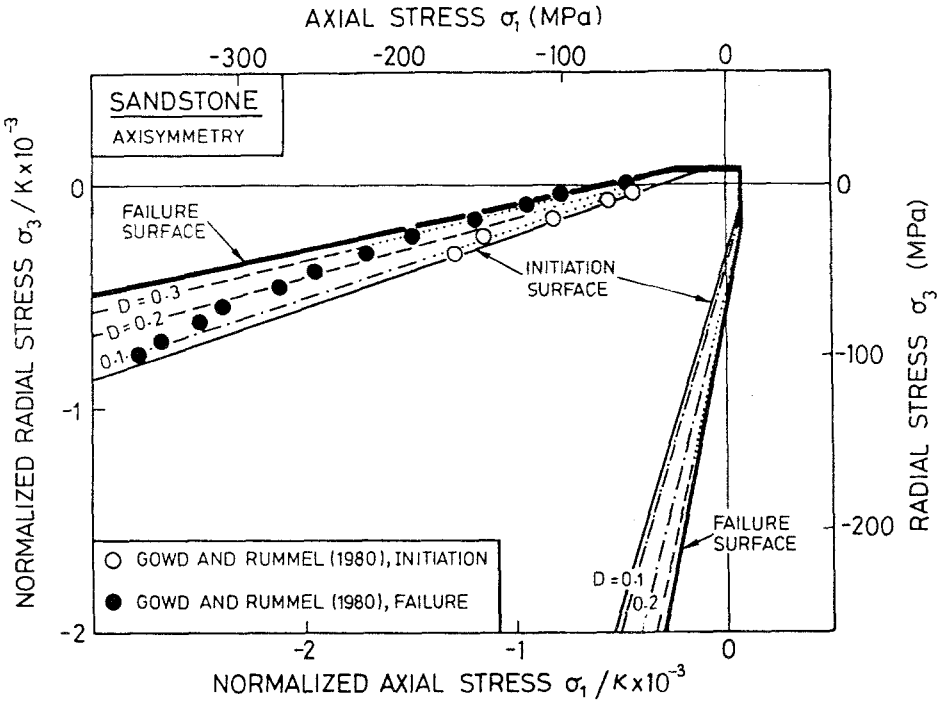

Figure 18
Comparison between experimental and theoretical failure surfaces for sandstone. The heavy solid line is the theoretical failure surface. The light solid line is the surface for the initiation of microfracturing while the light broken lines are surfaces of constant damage. The heavy broken line is the yield surface (eq. 30).

4.8. Marble

The only marble for which fracture initiation data is available is described by BRACE *et al.* (1966) as a medium grained almost pure calcite marble of unknown origin. They report it to be apparently isotropic, very ductile even at low confining pressures, with a grain size of about 0.2 mm.

The unusually low fracture initiation stress (Figure 20) requires either large starter flaws ($\sim$6 mm) or a low fracture toughness. Since ATKINSON and MEREDITH (1987a) report K_{Ic} as low as 0.19 MPa $m^{1/2}$ for calcite, we have fitted the initiation data using this value which then implies a starter flaw size of 0.4 mm, which is comparable to the grain size.

In a microscopic study of nucleation in marble, OLSSON and PENG (1976) found that microcracks often nucleate where slip bands intersect grain boundaries. Although such slip bands are physically analogous to angle cracks, there may be a significantly larger number of such nuclei since every favorably aligned grain is a

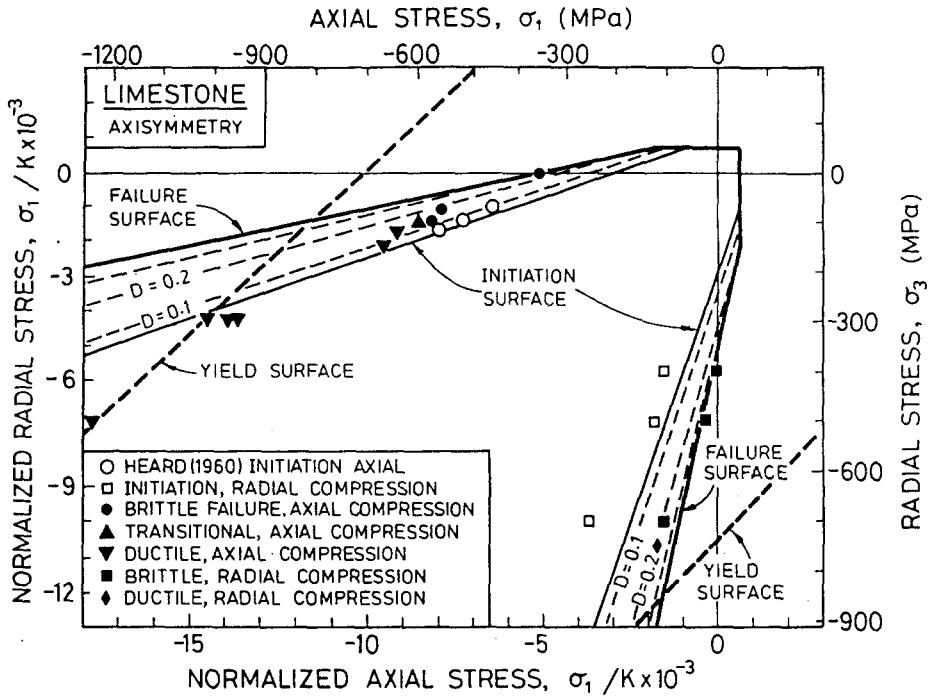

Figure 19

Comparison between experimental and theoretical failure surfaces for limestone. The heavy solid line is the theoretical failure surface. The light solid line is the surface for the initiation of microfracturing while the light broken lines are surfaces of constant damage. The heavy broken line is the yield surface (eq. 30).

potential source of nuclei. This may explain the large values of initial damage D_0 required to fit the marble data.

The data set which we fit is for Carrara marble which is the fine grained (about 0.1 mm) isotropic marble used by Michelangelo for the Pieta and other well-known works. Its total porosity is about 1.1% (EDMOND and PATERSON, 1972). The triaxial data in Figures 21 and 22 are from VON KARMAN (1911) and EDMOND and PATERSON (1972). Brittle versus ductile behavior was deduced from the shape of the stress-strain curve and from the volume changes associated with the deformation.

4.9. Rock Salt

Rock salt exhibits a room-temperature brittle-to-ductile transition at the lowest confining pressure of any rock in this study. HUNSCHE (1984) tested three types of natural salt at low confining pressure under both the common triaxial loading and the less common true multiaxial loading at strain rates of about $10^{-6}\,s^{-1}$. HANDIN

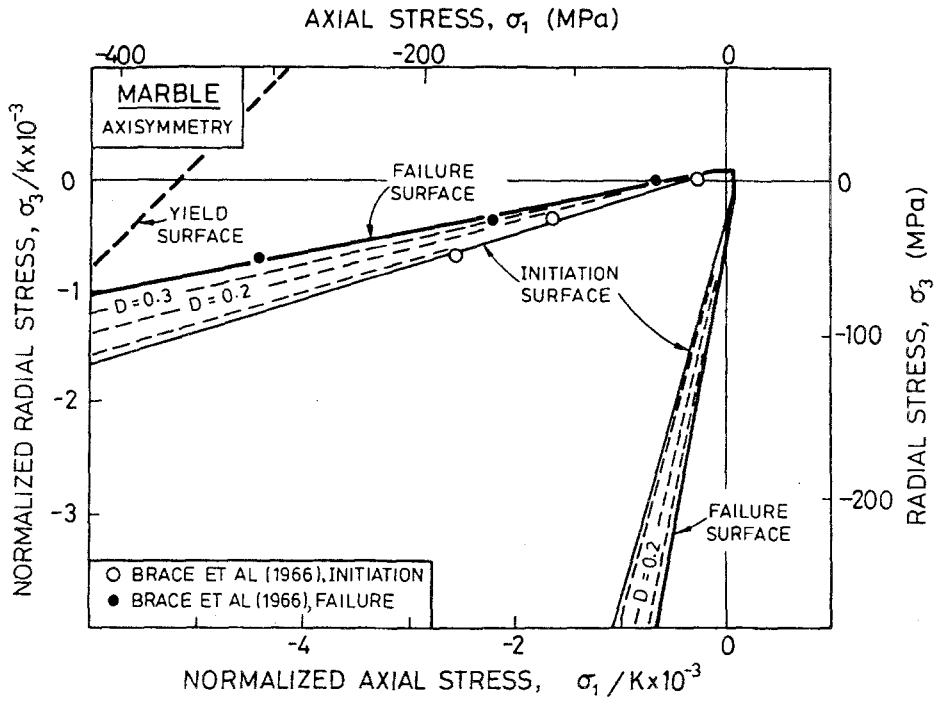

Figure 20

Comparison between experimental and theoretical failure surfaces for marble at low and intermediate confining stress. The heavy solid line is the theoretical failure surface. The light solid line is the surface for the initiation of microfracturing while the light broken lines are surfaces of constant damage. The heavy broken line is the yield surface (eq. 30).

(1953) collected conventional triaxial data to higher confining pressures at a strain rate of about $10^{-4}\,s^{-1}$. These data are shown in Figures 23 and 24.

5. *Conclusions*

1. An approximate physical model for damage evolution in brittle solids under compressive stress states has been developed. The model is based on the growth of wing cracks from a population of small, inclined, starter cracks; and the interaction between them. The important variables of the problem are: the size, $2a$, of the initial inclined cracks, and the initial damage

$$D_0 = \tfrac{4}{3}\pi(\alpha a)^3 N_V.$$

The state of the material is measured by the current value of the damage

$$D = \tfrac{4}{3}\pi(l + \alpha a)^3 N_V$$

where l is the length of the wing cracks.

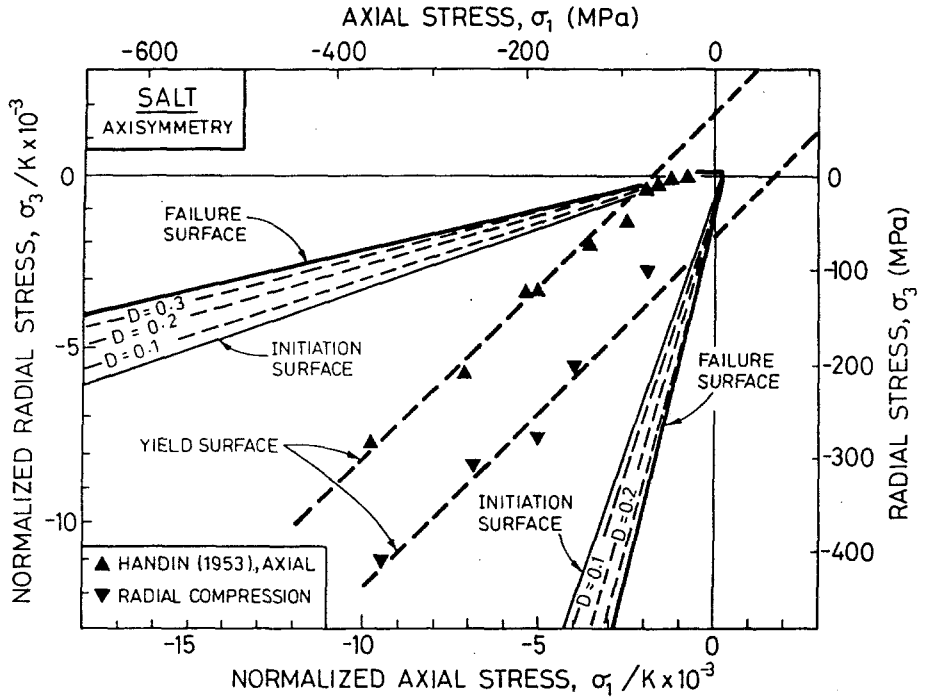

Figure 21
Comparison between experimental and theoretical failure surfaces for marble at low and intermediate confining stress. The heavy solid line is the theoretical failure surface. The light solid line is the surface for the initiation of microfracturing while the light broken lines are surfaces of constant damage. The heavy broken line is the yield surface (eq. 30).

We treat damage as a state variable. At the level of approximation of our treatment, the surfaces of constant damage in stress space are linear; this is primarily a consequence of our simplifying assumption that the population of initial cracks all have the same size. The surface corresponding to final macroscopic fracture is not one of constant damage (as often assumed). The terminal damage itself depends on the stress state, but it, too, is well approximated by a linear relationship:

$$\sigma_1 = C_2\sigma_3 - \sigma_c$$

where σ_c is the simple compressive strength.

The assumption that the initial fractures all have the same size does not affect the predicted (and observed) result that the combination of stresses corresponding to the first increment of new damage is linear, described by:

$$\sigma_1 = C_1\sigma_3 - \sigma_0.$$

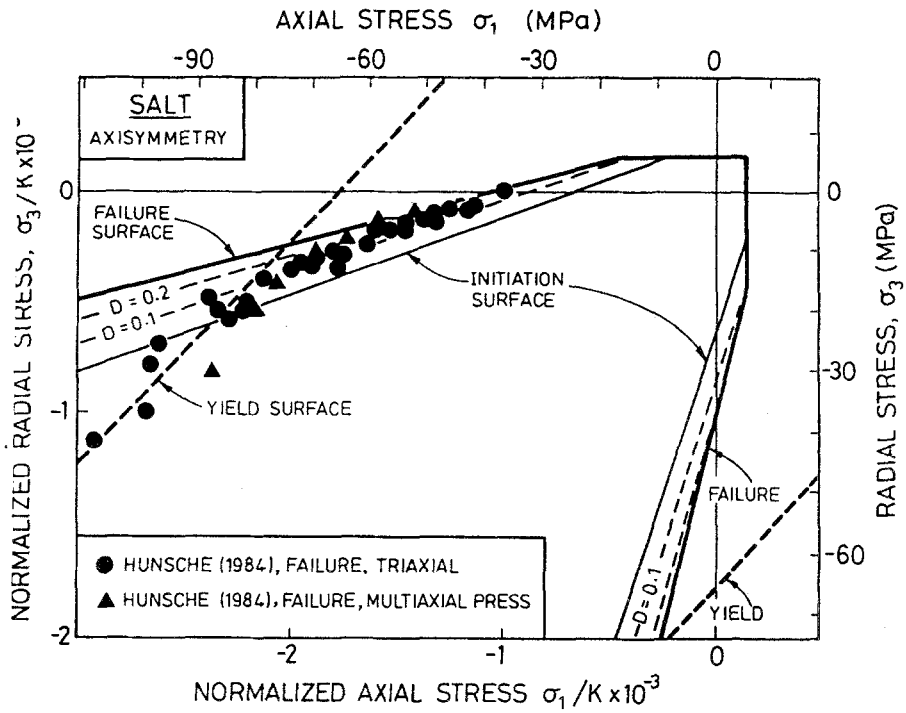

Figure 22

Comparison between experimental and theoretical failure surfaces for marble extended to the highest measured confining stress. The heavy solid line is the theoretical failure surface. The light solid line is the surface for the initiation of microfracturing while the light broken lines are surfaces of constant damage. The heavy broken line is the yield surface (eq. 30).

Damage always initiates at the largest flaws in the distribution, independent of the confining stress.

2. The model has been fitted to data for a number of rocks. The process gives physical insight into the damage accumulation and failure of these materials in compression. In particular, the fitting process leads to a value for the coefficient of friction across the crack faces, the size of the initial flaws, and the initial damage D_0. The failure process depends principally on these variables. Curvature of the failure surface is shown to depend, at least partly, on an interaction between the brittle failure mechanism and plastic flow. Rocks which show clearly established plasticity at high pressures (marbles, and rock salt, for example) show a brittle regime at low pressures, a transitional regime at intermediate pressures (both depending strongly on pressure), and a regime of plasticity at high pressures which is independent of pressure itself. It is noteworthy that silicate rocks such as granite, gabbro, dunite and aplite show a similar behavior, with the transition to plasticity dominating failure at confining pressures of general order E/30. This transition, at

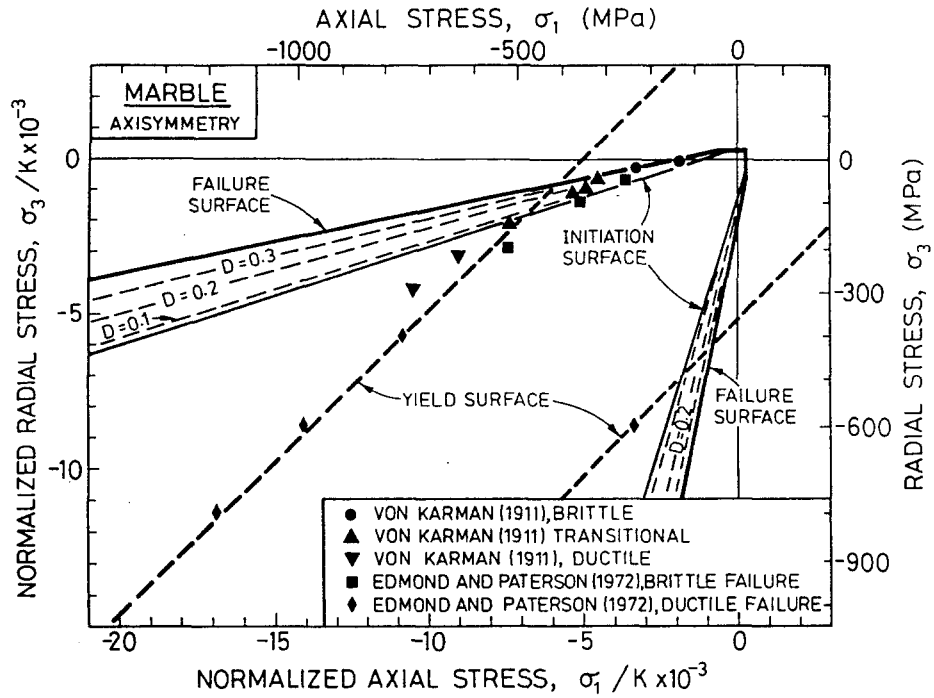

Figure 23

Comparison between experimental and theoretical failure surfaces for rock salt at low and intermediate confining stress. The heavy solid line is the theoretical failure surface. The light solid line is the surface for the initiation of microfracturing while the light broken lines are surfaces of constant damage. The heavy broken line is the yield surface (eq. 30).

first sight a surprising one, is nonetheless to be expected at such stress levels which are roughly the theoretical shear strength of the minerals within the rock.

Several other noteworthy conclusions emerge. One is that, in rocks which are almost fully dense, the initial flaw size is roughly equal to the grain size of the rock itself. But the initial damage level, D_0, varies widely. In low porosity crystalline silicates such as granite, this level is low (typically 3%); but in intrinsically-plastic materials like calcite and rock salt, the initial damage level is high (of order 15%) perhaps because the flaws from which wing cracks grow are slip bands within suitably oriented grains rather than cracks.

3. Data for rocks which are almost fully dense are well fitted by the model. We find, too, that porous rocks (limestone and sandstone, both with roughly 15% porosity) are also well fitted. This suggests that an analogous theoretical development may be possible for porosity induced cracking too.

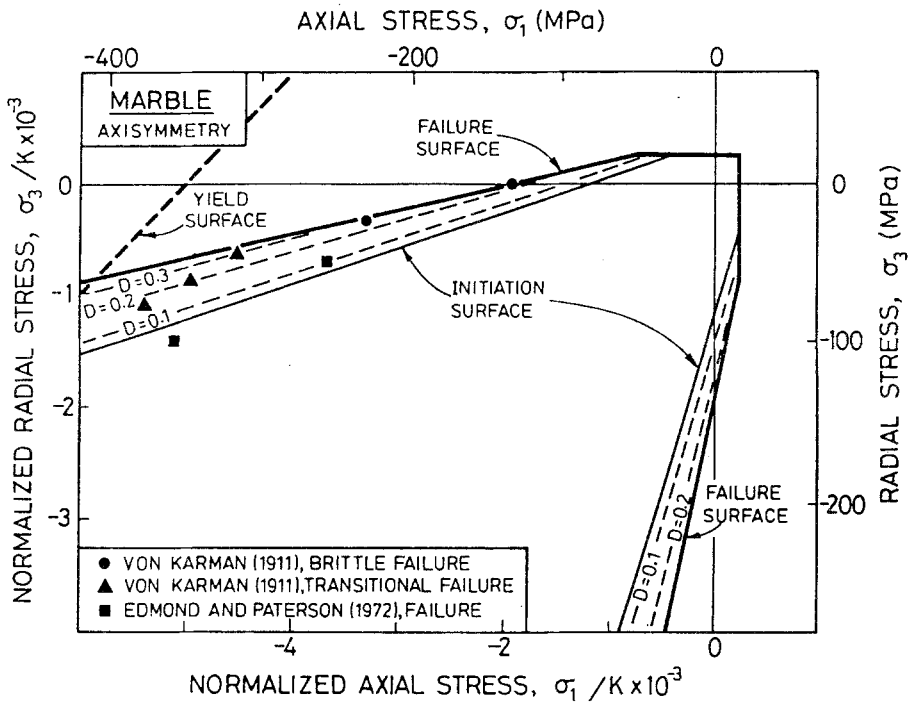

Figure 24

Comparison between experimental and theoretical failure surfaces for rock salt extended to the largest confining stress. The heavy solid line is the theoretical failure surface. The light solid line is the surface for the initiation of microfracturing while the light broken lines are surfaces of constant damage. The heavy broken line is the yield surface (eq. 30).

Acknowledgements

This work was supported by the United States Airforce DARPA contract # F19628-86-K-0003, and by the British Natural Environment Research Council, Contract GR3/6154A.

References

ANDERSON, O. L., and GREW, P. (1976), *Stress Corrosion Theory of Crack Propagation with Applications to Geophysics*, Rev. Geophys. Space Phys. *15*, 77–104.

ASHBY, M. F., and HALLAM S. D. (1986), *The Failure of Brittle Solids Containing Small Cracks under Compressive Stress States*, Acta Metall. *34*, 497–510.

ATKINSON, B. K., and MEREDITH, P. G., *Experimental fracture mechanics data for rocks and minerals*, In *Fracture Mechanics of Rock* (ed. Atkinson, B. K.) (Academic Press, New York 1987a) pp. 477–525.

ATKINSON, B. K., and MEREDITH, P. G., *The theory of subcritical crack growth with applications to minerals and rocks*, In *Fracture Mechanics of Rock* (ed. Atkinson, B. K.) (Academic Press, New York 1987b) pp. 111–166.

BIRCH, F. (1960), *The Velocity of Compressional Waves in Rocks to 10 Kilobars, Part 1*, J. Geophys. Res. *65*, 1083–1102.

BRACE, W. F., PAULDING, B. W., and SCHOLZ, C. (1966), *Dilatancy in the Fracture of Crystalline Rocks*, J. Geophys. Res. *71*, 3939–3953.

COSTIN, L. S. (1983), A *Microcrack Model for the Deformation and Failure of Brittle Rock*, J. Geophys. Res. *88*, 9485–9492.

COSTIN, L. S. (1985), *Damage Mechanics in the Post-failure Regime*, Mechanics of Materials *4*, 149–160.

COSTIN, L. S., and HOLCOMB, D. J. (1981), *Time-dependent Failure of Rock under Cyclic Loading*, Tectonophysics *79*, 279–296.

EDMOND, J. M., and PATERSON, M. S. (1972), *Volume Changes During the Deformation of Rocks at High Pressures*, Int. J. Rock Mech. Min. Sci. *9*, 161–182.

GOWD, T. N., and RUMMEL, F. (1980), *Effect of Confining Pressure on the Fracture Behavior of a Porous Rock*, Int. J. Rock Mech. Min. Sci. and Geomech. Abstr *17*, 225–229.

GRIFFITH, A. A., *Theory of rupture*, In *Proc. First International Congress Applied Mechanics* (Delft 1924) pp. 55–63.

GRIGGS, D. T., and HANDIN J., *Observations on fracture and a hypothesis of earthquakes*, In *Rock Mechanics* (eds. Griggs, D. T., and Handin, J.) (Geol. Soc. Am. Memoir *79* 1960) pp. 347–364.

HALLBAUER, D. K., WAGNER, H., and COOK, N. G. W. (1973), *Some Observations Concerning the Microscopic and Mechanical Behaviour of Quartzite Specimens in Stiff, Triaxial Compression Tests*, Int. J. Rock Mech. Min. Sci. *10*, 713–726.

HANDIN, H. (1953), *An Application of High Pressure in Geophysics: Experimental Rock Deformation*, Trans. Am. Soc. Mech. Engrs. *75*, 315–324.

HEARD, H. C., *Transition from brittle fracture to ductile flow in Solenhofen limestone as a function of temperature, confining pressure, and interstitial fluid pressure*, In *Rock Deformation* (eds. Griggs, D., and Handin, J.) (Geol. Soc. Am. Memoir *79* 1960) pp. 193–226.

HOLCOMB, D. J., and COSTIN, L. S. (1986), *Damage in brittle materials: Experimental methods*, In *Proceedings of the Tenth U.S. National Congress of Applied Mechanics* (ed. Lamb, J. P.) pp. 107–113.

HORII, H., and NEMAT-NASSER, S. (1985), *Compression-induced Microcrack Growth in Brittle Solids: Axial Splitting and Shear Failure*, J. Geophys. Res. *90*, 3105–3125.

HORII, H., and NEMAT-NASSER, S. (1986), *Brittle Failure in Compression: Splitting, Faulting and Brittle-ductile Transition*, Phil. Trans. Roy. Soc. *A319*, 337–374.

HUNSCHE, U., *Fracture experiments on cubic rock salt samples*, In *Mechanical Behaviour of Salt* (eds. Hardy, H. R., Jr., and Langer, M.) (Trans. Tech. Publications, Clausthal, Germany 1984) pp. 169–179.

IRWIN, G. R., *Fracture*, Handbuch der Physik, Vol. 6 (Springer, Berlin 1958) pp. 551–590.

JAEGER, J. C., and COOK, N. G. W., *Fundamentals of Rock Mechanics*, 2nd Ed. (Chapman and Hall, London 1976).

JANACH, W., and GUEX, L. H. (1980), *In-plane Propagation of Shear Microcracks in Brittle Rocks under Triaxial Compression*, J. Geophys. Res. *85*, 2543–2553.

KEMENY, J., and COOK N. G. W., *Crack models for the failure of rocks in compression*, In *Constitutive Laws for Engineering Materials: Theory and Applications* (ed. Desai, C. S.) (Elsevier 1987) pp. 879–887.

KNOTT, J. F., *Fundamentals of Fracutre Mechanics* (Butterworths, London 1973).

MARTIN, R. J. (1972), *Time-dependent Crack Growth in Quartz and its Application to the Creep of Rocks*, J. Geophys. Res. *77*, 1406–1419.

MOGI, K. (1966), *Some Precise Measurements of Fracture Strength of Rocks under Uniform Compressive Stress*, Rock Mech. Eng. Geol. *4*, 41–55.

NEMAT-NASSER, S., and HORII, H. (1982), *Compression Induced Nonplanar Crack Extension with Application to Splitting, Exfoliation, and Rockburst*, J. Geophys. Res. *87*, 6805.

NEWMAN, J. B. (1978), *A failure model for concrete*, In *Developments in Concrete Technology — 1* (ed. Lydon, F. D.) Applied Science *5*, 151–160.

OLSSON, W. A., and PENG, S. S. (1976), *Microcrack Nucleation in Marble*, Int. J. Rock Mech. Min. Sci. and Geomech. Abstr. *13*, 53–59.

PATERSON, M. S., *Experimental Rock Deformation — The Brittle Field* (Springer-Verlag, New York 1978).

RUTTER, E. H. (1972), *The Effects of Strain-rate Changes on the Strength and Ductility of Solenhofen Limestone at Low Temperature and Confining Pressures*, Int. J. Rock Mech. Min. Sci. and Geomech. Abstr. *9*, 183–189.

SAMMIS, C. G., and ASHBY, M. F. (1986), *The Failure of Brittle Porous Solids under Compressive Stress States*, Acta Metall. *34*, 511–526.

SANO, O., ITO, I., and TERADA, M. (1981), *Influences of Strain Rate on Dilatancy and Strength of Oshima Granite under Uniaxial Compression*, J. Geophys. Res. *86*, 9299–9311.

SCHOCK, R. N., and HEARD, H. C. (1974), *Static Mechanical Properties and Shock Loading Response of Granite*, J. Geophys. Res. *79*, 1662–1666.

SCHOLZ, C. H., *A short geophysical history of Westerly granite*, Preface to *Earthquake Source Mechanics* (eds. Das, S., Boatwright, J., and Scholz, C. H.) (Am. Geophys. Union Monograph *37* 1986) p. ix.

SHIMADA, M. (1981), *The Method of Compression Test under High Pressures in a Cubic Press and the Strength of Granite*, Tectonophysics *72*, 343–357.

SHIMADA, M., CHO, A., and YUKUTAKE, H. (1983), *Fracture Strength of Dry Silicate Rocks at High Confining Pressures and Activity of Acoustic Emission*, Tectonophysics *96*, 159–172.

TADA, H., PARIS, P. C., and IRWIN, G. R., *The Stress Analysis of Cracks Handbook* (Del Res., St. Louis, Mo. 1985).

TOPPONNIER, P., and BRACE, W. F. (1976), *Development of Stress-induced Microcracks in Westerly Granite*, Int. J. Rock Mech. Min. Sci. *13*, 103–112.

VON KARMAN, T. (1911), *Festigkeitsversuche unter allseitigem Druck*, Z. Ver. Dt. Ing. *55*, 1749–1757.

WAWERSIK, W. R., and FAIRHURST, C. (1970), *A Study of Brittle Rock Failure in Laboratory Compression Experiments*, Int. J. Rock Mech. Min. Sci. *7*, 561–575.

WAWERSIK, W. R., and BRACE W. F. (1971), *Post-failure Behavior of a Granite and a Diabase*, Rock Mech. *3*, 61–85.

WAZA, T., KURITA, K., and MIZUTANI, H. (1980), *The Effect of Water on the Subcritical Crack Growth in Silicate Rocks*, Tectonophysics *67*, 25–34.

(Received January 12, 1989, accepted September 30, 1989)